

Effect of the cross-section architecture on the impact resistance of bio-inspired low-porosity structures using neural networks

Shashank Kushwaha¹, Junyan He¹, Diab Abueidda², Iwona Jasiuk^{1*}

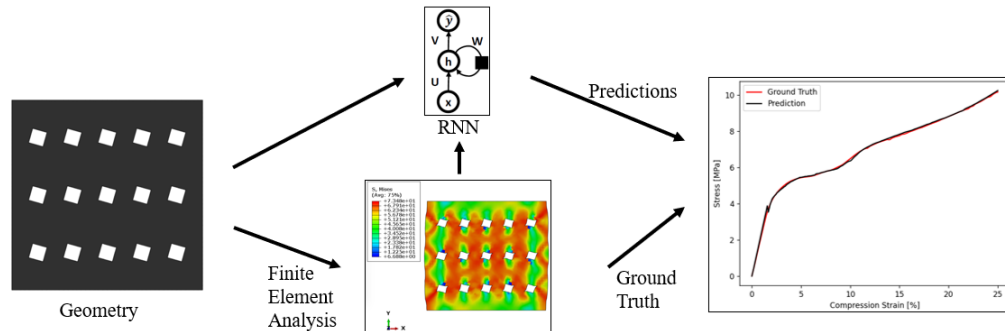
¹ Department of Mechanical Science and Engineering, University of Illinois at Urbana-Champaign, Urbana, IL, USA

² National Center for Supercomputing Applications, University of Illinois at Urbana-Champaign, Urbana, IL, USA

Abstract

Biological structural designs in nature, like hoof walls, horns, and antlers, can be used as inspiration for generating structures with excellent mechanical properties. A common theme in these designs is the small percent porosity in the structure ranging from 1 - 5%. In this work, the sheep horn was used as an inspiration due to its higher toughness when loaded in the radial direction compared to the longitudinal direction. Under dynamic transverse compression, we investigated the structure-property relations in low porosity structures characterized by their two-dimensional (2D) cross-sections. A diverse design space was created by combining polygonal tubules with different numbers of sides placed on a grid with different numbers of rows and columns. The volume fraction and the orientation angle of the tubules were also varied. The finite element (FE) method was used with a rate-dependent elastoplastic material model to generate the stress-strain curves in plane strain conditions. A gated recurrent unit (GRU) model was trained to predict the structures' stress-strain response and energy absorption under different strain rates and applied strains. The parameter-based model uses eight discrete parameters to characterize the design space and as inputs to the model. The trained GRU model can efficiently predict the response of a new design in as little as 0.16 ms and allows rapid performance evaluation of 128000 designs in the design space. The GRU predictions identified high-performance structures and four design trends that affect the specific energy absorption were extracted and discussed.

Graphical abstract



*Corresponding author

Email address: ijasiuk@illinois.edu (Iwona Jasiuk¹)

Keywords: Bio-Inspired, Structure-property relations, Neural networks, Specific energy absorption

1. Introduction

Lightweight structures with high energy absorption capacity are of high interest for multiple engineering applications. Various structural elements found in animals and plants could be used as inspiration to design novel structures that can sustain impacts generated during collision [1–3]. The process of evolution has created complex architectures in nature capable of handling low-to-medium velocity impacts (up to 50 m/s). An example is the trabecular-honeycomb biomimetic structure inspired by beetle elytra [4]. Rams see impact velocities of around 5.5 m/s when fighting. Also, sheep horn can withstand a maximum impact force of 3400N [5] during collisions. Biological structures exhibit excellent energy absorption capabilities and inspire the design of new energy absorbers. Bio-inspired structures have been used in countless applications, including automobiles [6], protective armors [7], and wings of aircraft [8]. Further, a variety of materials have been used to manufacture bio-inspired structures, including polymers [9], aluminum alloy [6], fiber-reinforced composites [10], and concrete [11]. Hence, studying the structure-property relations of bio-inspired designs is of great research and industrial interest. The exploration of structure-property relations involves surveying many different structural features at a given loading condition. Various studies utilize optimization-based methods to generate new designs for energy absorption and study the structure-property relations [12–15]. However, a systematic compilation of bio-inspired designs' mechanical response and energy absorption characteristics is lacking. This paper aims to develop a systematic framework to generate structures that combine different design elements found in low-porosity structures in nature. i.e., the study of the structures with aligned tubules whose porosity is in the range of 1% - 5%, under transverse dynamic compression. The framework generates low porosity structures with constant cross-sections along the thickness direction by randomly combining various design features such as tubule shape, orientation, and in-plane arrangement.

Neural network (NN) models have been extensively used in the field of mechanics to predict stress-strain response in composites [16–18], metals [19–21], and lattices [22–24]. However, the use of NN models for studying bio-inspired structures remains scarce. Once trained, the NN can efficiently predict the mechanical performance of new designs at a rate much faster than classical numerical simulations, thus allowing rapid preliminary design selection and trend identification. Therefore, the second objective of this work is to develop a neural network (NN) model to approximate the structure-property relations, linking the input design parameters with loading conditions and the mechanical performance of the structure. Using this trained model, structure-property maps of the design space at different loading rates are identified, and design trends are discussed.

This paper is organized as follows: Section 2 presents an overview of the numerical simulations, the input data preprocessing, and the NN model's architecture. Section 3 includes the results obtained from the study, and explores the quality of NN predictions and the validity of the results. Section 4 summarizes the outcomes and lists some possible future directions for the bio-inspired structures.

2. Methods

2.1. Geometry generation and Finite element analysis

The designs considered in this work are 3D structures containing tubules with a constant cross-section; hence the designs can be uniquely characterized by their 2D, in-plane cross-sections, and the plane strain condition is assumed. A Python script was developed to generate cross-sectional sketches in the finite element (FE) analysis package Abaqus [25] for a given volume fraction, tubule shape, tubule orientation, and the arrangement of the tubules within the structure. The cross-section of the bio-inspired structures studied in this work is an 11-by-11 mm² square, whereas all the tubules are confined within a concentric square area of 10-by-10 mm². The tubule volume fraction was uniformly sampled from the range [1% , 5%]. In this work, we approximated the tubule cross-sections by polygons of a different number of sides that were uniformly sampled from the range [3, 6]. Additional rotation was applied to the cross-sections, and the rotation angle was uniformly sampled from the range [0, 360] degrees. Multiple tubules can be present in the structure, and we placed them on a $n_y \times n_x$ grid, where n_y and n_x denote the number of rows and columns, respectively. n_y and n_x were sampled in the range [1, 8]. Some selected structures in the design space are shown in Fig. 1. All the structures were discretized with 4-node bilinear plane strain quadrilateral elements with reduced integration. A nominal element edge length of 0.24 mm was chosen for meshing.

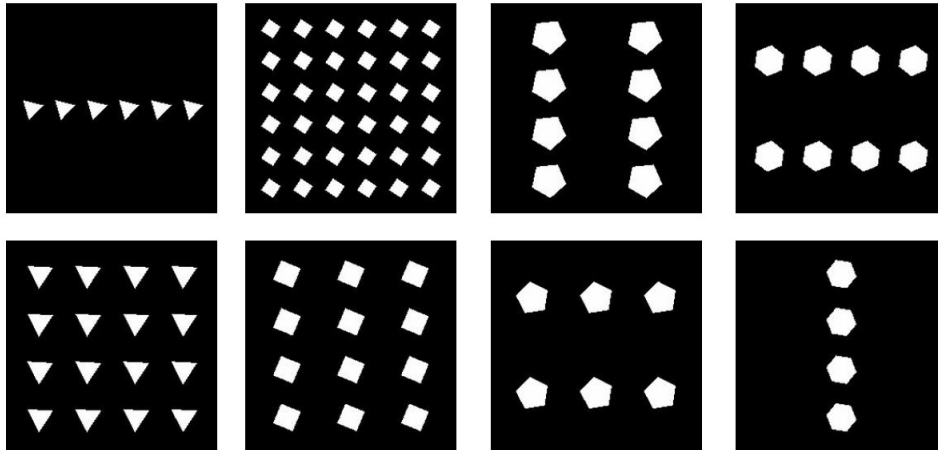


Figure 1: Sample structures in the design space

The relationship between different structural designs and energy absorption mechanisms seen in bones, teeth, and horns is discussed by McKittrick et al.[26]. Further, they discuss that when rams butt heads, the horns are loaded in the transverse direction, which provides more energy absorption than in the longitudinal direction. The Abaqus/Explicit dynamic simulation defined a rate-dependent elastic-plastic material model to capture the structures' response at varying strain rates. The material properties of the base material chosen for the study are similar to polycarbonate-acrylonitrile butadiene styrene (PC-ABS). The Young's modulus and Poisson's ratio are 2.5 GPa and 0.35, respectively. The strain rate dependent yield stress versus plastic strain curves used to define the plastic region are included in Fig. 2. However, the strains to failure are tremendous in horns, as much as 80%. Hence, no damage model has been used in this study since the maximum nominal strain considered is 25%.

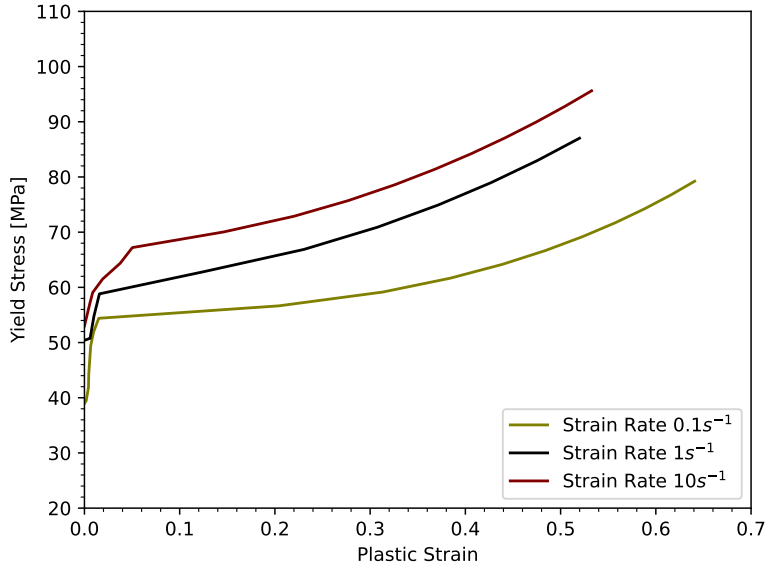


Figure 2: Yield Stress versus Plastic Strain at different strain rates

In this study, the boundary conditions for impact loading were approximated by sandwiching the structure between two rigid plates, and the structures were subjected to dynamic transverse compression. The bottom plate was held fixed, and the top plate traveled downward with a constant velocity determined by the user-defined strain rate. The nominal strain rate was uniformly sampled from the range $[0.9, 90.9] \text{ s}^{-1}$ corresponding to indenter velocity from the range $[10, 1000] \text{ m/s}$. The reaction force and displacement were measured at the top rigid plate. All sidewalls were traction-free and were free to deform. All simulations had a constant final displacement of 2.25 mm, corresponding to 25% nominal compressive strain along the y-axis. The reaction force and displacement at the top plate, plastic dissipation, and elastic strain energy of the porous structures were outputs of the FE simulations. Fig. 3 depicts the FE model assembly and a typical deformed structure at the end of dynamic compression. A total of 4500 simulations were conducted on an AMD Ryzen 7 5800H processor with 8 cores. Depending on the applied impact velocity, each simulation took about 5-30 minutes to complete.

2.2. Neural network for sequence prediction

2.2.1. Input data, data augmentation, and loss function

The input parameter range is described in Section 2.1. The corresponding output arrays were obtained from the impact simulations conducted in Abaqus/Explicit. The output arrays were down-sampled to 50-time steps for the efficiency of neural network training. The inputs used in the model consist of eight temporal information arrays. The first five arrays are constant in time and correspond to the parameters used to define the structure's geometry. The parameters include n : the topology of the tubule (i.e., number of sides in a polygon), n_x : number of tubules evenly distributed in the x direction, n_y : number of tubules evenly distributed in y direction, a_0 : rotation angle for all the tubules in the structure, and v_f : volume fraction of the individual tubule in each element created

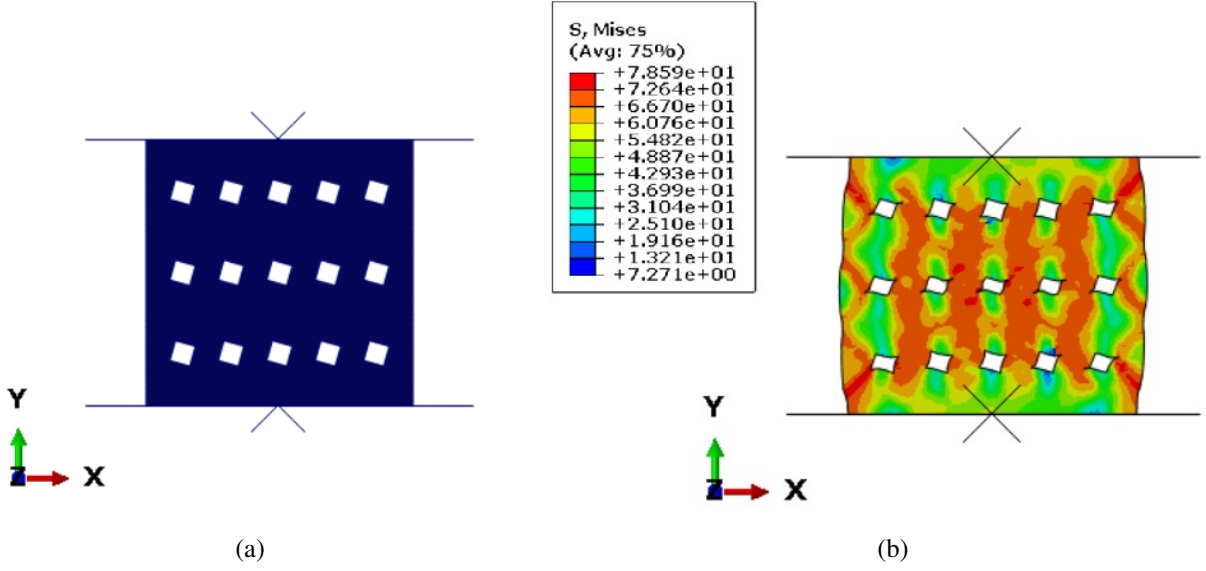


Figure 3: FE model setup and results: (a) Typical structure with two rigid plates for dynamic transverse compression. (b) A typical deformed structure showing von Mises stress.

by n_x times n_x elements in a 10-by-10 mm² grid. The remaining three inputs are physics-informed temporal arrays described as follows:

1. Current time value at each output time point.
2. Nominal compression strain at each output time point.
3. Nominal compression strain rate.

A standard scaler in Scikit-Learn normalized all the inputs [27] before training. The scaler was fitted only to the training data points to avoid information leakage [16]. The available training data was increased using data augmentation. Corresponding to each simulation conducted in Abaqus with 25% final nominal strain, twenty final nominal strains in the range [10%,25%] were randomly sampled, and all inputs and outputs were linearly interpolated to the selected final strain level. This method generated training data points at the same strain rate but different final nominal strain, and increased the total number of input data points from 4500 to 90000. These data points were divided into training (65%), validation (15%), and testing datasets (20%).

The mean absolute error (MAE) has been employed as the loss function in this study [28]. The loss function is defined as:

$$\text{MAE} = \frac{\sum_{i=1}^N |\mathbf{Y}_i - \hat{\mathbf{Y}}_i|}{N}, \quad (1)$$

where N , \mathbf{Y}_i , $\hat{\mathbf{Y}}_i$ denote the number of training data points, ground-truth outputs, and the NN predictions, respectively. The mean squared error (MSE) is chosen as a metric, which is defined as:

$$\text{MSE} = \frac{\sum_{i=1}^N (\mathbf{Y}_i - \hat{\mathbf{Y}}_i)^2}{N}. \quad (2)$$

2.2.2. Neural network model

This study uses a recurrent neural network (RNN) model to train the forward model for output prediction. Specifically, the gated recurrent unit (GRU) model is used. This model has been widely used to predict sequences [29–32]. Further, Abueidda et al.[30] compared the performance of different RNN models to predict the response of elastoplastic material undergoing deformation under variable strain rates. Although the GRU model is more computationally expensive than the long short-term memory (LSTM) model and the temporal convolutional network (TCN) model, it predicts the output with lower error. Based on the GRU model’s demonstrated capabilities to predict the structures’ response under complex deformation histories, this study used the model to predict stress-strain curves for the structures under dynamic transverse compression.

The GRU-based model was implemented and tested in Keras [33] with a TensorFlow [34] backend. The GRU model comprises three stacked layers of 500 GRU units, each with hyperbolic tangent (tanh) activation leading to a model with 3.77 million trainable parameters. The loss function was minimized using an Adam optimizer [35] with an initial learning rate of 1×10^{-3} . The model was trained for 150 epochs with a batch size of 600, and training was repeated 10 times to obtain average training time and model accuracy. The data set was shuffled and partitioned in each training repetition, as described in Section 2.2.1. All training was conducted on Google Colab Pro+ using GPU acceleration on Tesla V100 GPU.

2.3. Global optimization

Using the trained neural network, a Python script was developed to traverse the input design space and evaluate the energy absorption performance. The input design space was divided into grid points based on the first five input parameters described in Section 2.2.1. Each grid point represents a unique structure within the input design space based on five input parameters. The specific energy absorption (SEA) was computed for each grid point by calculating the area under the load-displacement curve (calculated from the GRU model predictions). Three design parameters: side of the polygon, n_x and n_y could take discrete integer values within their respective input range, whereas volume fraction and angle offset were divided into 40 and 20 equally spaced intervals, respectively. Hence, this method was used to analyze the SEA for 128000 structures within the input design space. However, it should be noted that only the designs with non-intersecting tubules are considered valid. Other designs are excluded from the analysis. This process was repeated for five different values of v_y within the range described in Section 2. A similar process can be repeated at different equally spaced intervals to obtain the performance of all the structures in the input design space for a given set of final strain and velocity of the indenter (v_y).

3. Results and discussion

3.1. Predicting stress-strain curves and energy outputs

The number of input data points used in training was decided based on the prediction accuracy measured using the value of the loss function. In this study, the percentage of total input data was incremented to train the neural network model until similar prediction accuracy was observed. Further, the average response of the GRU model was measured by training the model 10 times after shuffling the data before each training iteration. The loss function value corresponding to the increasing amount of training data is shown in Fig. 4a. Further, a typical training history is also

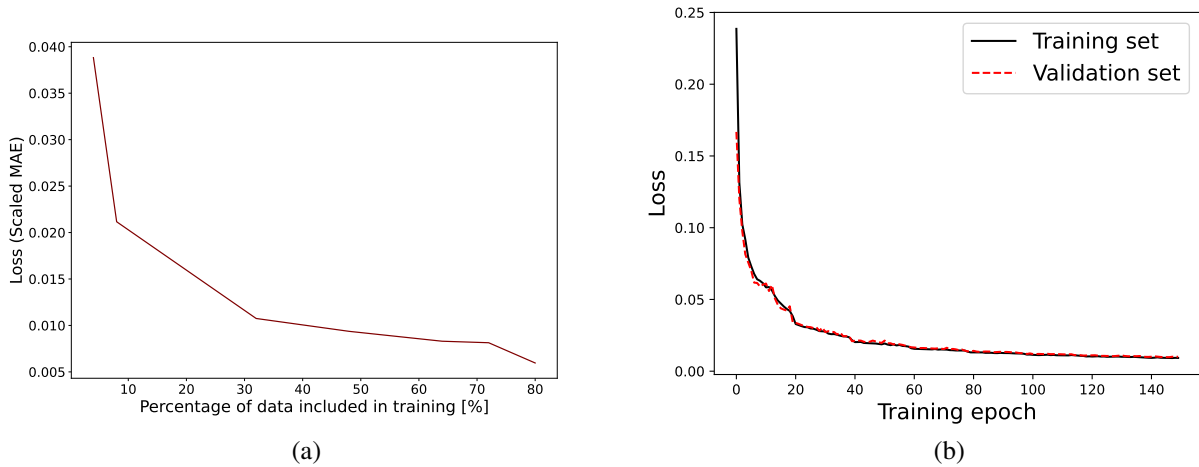


Figure 4: Convergence plot for GRU model training process: (a) Scaled mean squared error when a different percentage of the total data is used in training. (b) Scaled mean absolute error evolution during training. Note that the MAE shown here is the MAE computed on the variables scaled by the standard scaler.

Table 1: Computational cost for GRU training, inference, and FE simulations

	GRU training	GRU inference	FE simulation
Time	5192.9s	1.63×10^{-4} s	5-30 mins ¹

presented in Fig. 4b. The average training and inference times for the GRU model and the average FE simulation time are reported in Table 1.

After training the NN, the NN predictions were compared to the ground truths obtained from FE simulations, ranked by the percentile of MAE for each output array. The model with median MAE among the 10 training repetitions was used to generate the plots shown in Fig. 5. The final MAE for this model is 6.07×10^{-3} . The amount of data required for training was chosen by checking the loss function value for different percentages of input data. Fig. 4a shows that the loss increases as the percentage of the input data is decreased concerning the reference (80% data). Hence, we chose 80% data as input for training. Further, it could be inferred from Fig. 4b that no major overfitting has occurred. The statistical distribution of MAEs is shown in Fig. 5. From the first three columns, up to 75% percentile, we could see that the GRU model can closely predict the FE simulation results for stress-strain curves, plastic dissipation, and elastic strain energy. Even in the worst case, the GRU model correctly predicts the general shape of the FE-simulated stress-strain curve.

In the current study, the cross-section image of the structure has been parameterized using five design variables. These variables are then used as inputs in the GRU model. Another valid approach is to encode the cross-sectional images of the design via an autoencoder before training the GRU model. This approach was used in the work of He et al.[29] for exploring the structure-property relations of thin-walled lattices. However, training the autoencoder can take additional computational resources and is unnecessary when discrete parameter values can parameterize the current design space. Hence in this work, we used the design parameters to describe the designs

¹Depends on the impact velocity of the rigid plate. A lower impact speed leads to a longer solution time due to the small time step size used in the explicit analysis.

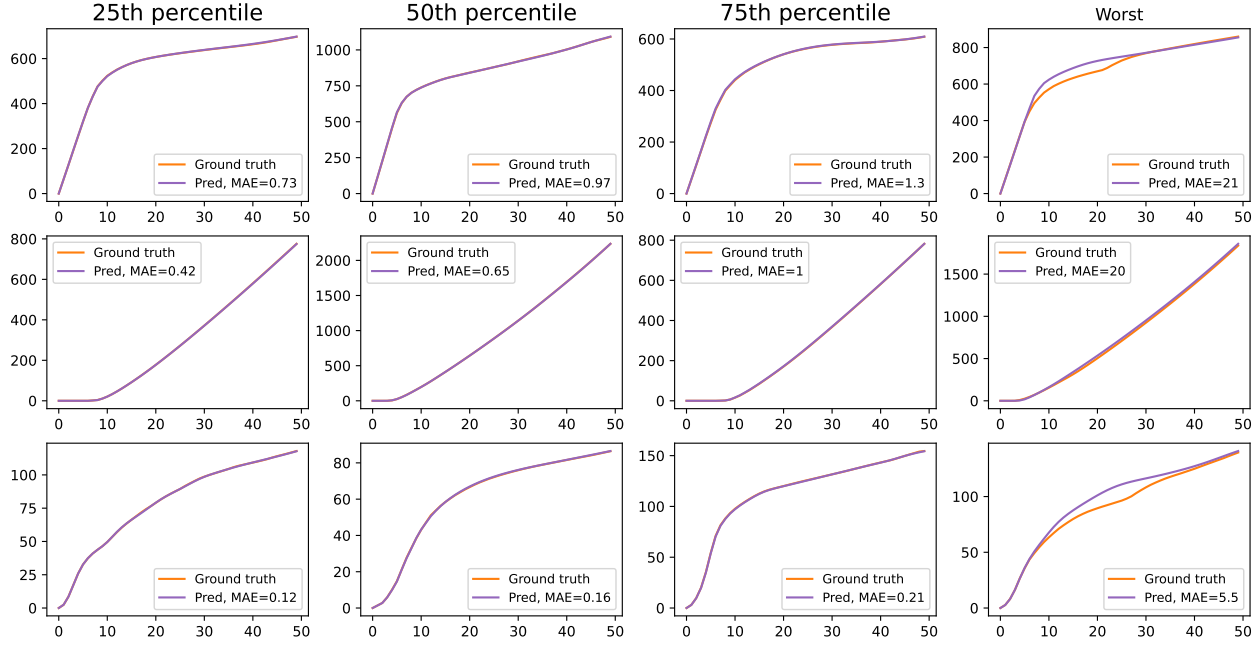


Figure 5: Comparison of ground truths and GRU predictions for the data set, ranked by percentile of MAE to provide a representative sampling. Here, MAE is ranked independently for each of the four output arrays.

instead of the autoencoder. However, judging from the comparison with FE data shown in Fig. 5, the prediction accuracy is high even with the simplified approach.

3.2. Validation of the neural network predictions

The worst and best designs (as predicted by the trained GRU model) at two different impact velocities (10 and 100 m/s) were validated by FE simulations to check the accuracy of the GRU model predictions. The four designs are depicted in Fig. 6. FE simulations were conducted to obtain the ground-truth values of SEA under an applied plate velocity of 10 m/s (cases (a) and (b)) and 100 m/s (cases (c) and (d)) and a final axial strain of 0.25. The comparison of the FE-simulated and GRU-predicted SEA values are shown in Fig. 7. As can be seen from the results, the trained GRU is highly accurate for the two impact velocities tested, and the predicted SEA values fall within 5% of their respective ground truth values. This result provides confidence in applying the trained model for further inference tasks.

3.3. Structure-SEA map

The Python script described in Section 2.3 was used to calculate SEA from the stress-strain curve predicted by the NN at each design point. Each structure could be represented by a unique design index defined using the first five input parameters to the NN as described in Section 2.2.1. Finally, the scatter plots for SEA at each design surveyed in the grid search for two different impact velocities are plotted in Fig. 8 and Fig. 9, which show a structure-property map for this chosen design space.

Using the scatter plot shown in Fig. 8, we could identify the best and worst designs regarding specific energy absorption within the input design space for the given loading condition and final

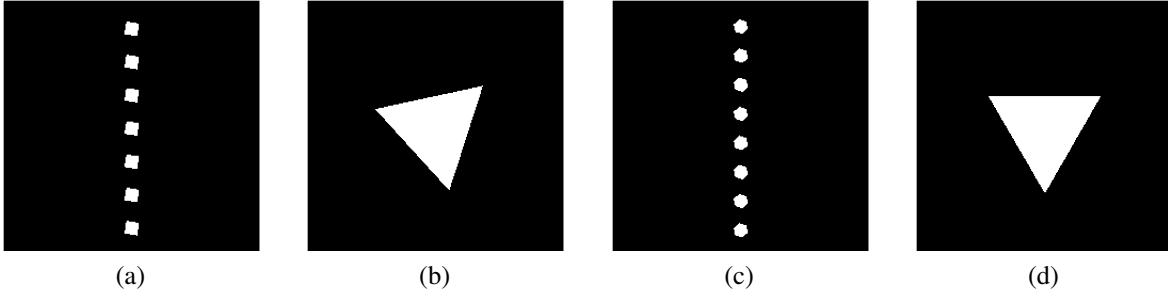


Figure 6: Highest and lowest SEA designs as predicted by the trained GRU model: (a) highest SEA, 10 m/s, (b) lowest SEA, 10 m/s, (c) highest SEA, 100 m/s, (d) lowest SEA, 100 m/s.

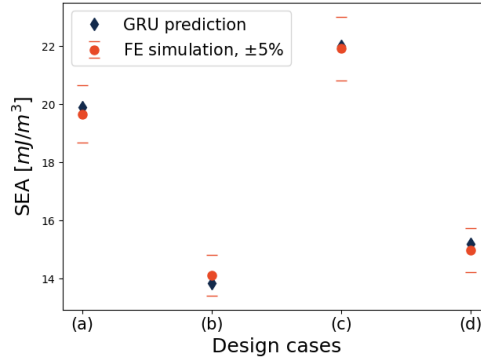


Figure 7: Comparison of the FE-simulated and GRU-predicted SEA values for the four validation design cases.

strain. These two points are also highlighted in the Fig. 8. Further, the same Python code described in Section 2.3 could be used to plot the SEA for structures with various constraints. For example, Fig. 10 shows the distribution of SEA for structures with a volume fraction of porosity between 4.5% and 5%.

3.4. Design trends and observations

The structure-energy absorption maps shown in Section 3.3 are useful for obtaining an overview of the entire design space. However, additional design insights could be drawn from the map to guide future design work:

1. At the same volume fraction of porosity within the structure, final strain, and indenter velocity exceeding 100 m/s, arranging the pores vertically results in optimal energy absorption. By contrast, the lowest energy absorption is achieved when the porosity is concentrated at the center. The structure illustrated in Fig. 11 emerged as the most efficient design for SEA, according to the SEA map depicted in Fig. 8. Conversely, the structure in Fig. 12 demonstrated the lowest SEA. The structure with maximum SEA (Fig. 11) has a porosity of close to 1%, whereas the one with minimum SEA (Fig. 12) has a porosity closer to 5%. In both instances, we observe a higher stress band that originates at the structure's corners and radiates toward its center during compression. In essence, the presence of material in areas of high stress is crucial for achieving a higher SEA. In the case of the structure in Fig. 11, only a few pores are present within the high-stress region. On the other hand, the structure illustrated

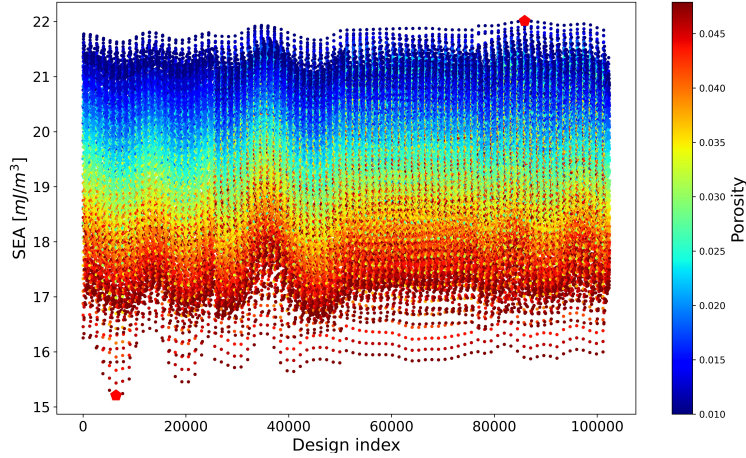


Figure 8: Structure-property relations at an impact velocity $v_y = 100\text{m/s}$ and final axial strain of 0.25. The highest and lowest SEA designs are highlighted in solid red pentagons.

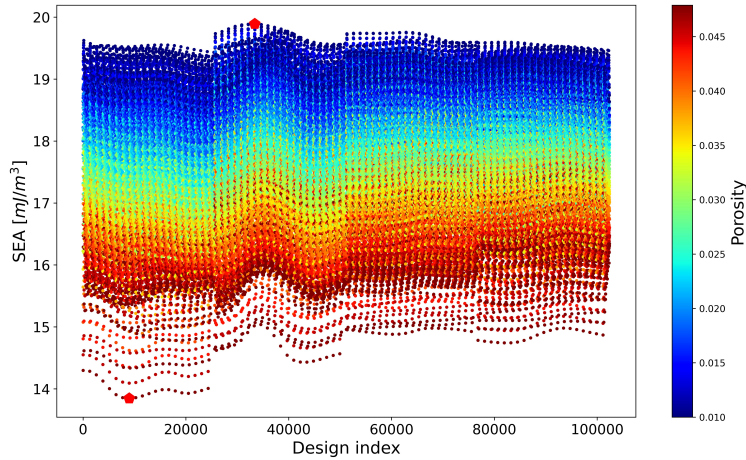


Figure 9: Structure-property relations at an impact velocity $v_y = 10\text{m/s}$ and final axial strain of 0.25. The highest and lowest SEA designs are highlighted in solid red pentagons.

in Fig. 12 has its entire porosity at the center, resulting in diminished load-carrying capacity and a lower SEA.

2. The orientation of polygonal tubules significantly impacts energy absorption in low-porosity structures. This can be observed in Fig. 13, which illustrates two structures with the same square-shaped porosity volume fraction but different angle offsets. When subjected to similar loading conditions, Fig. 13b exhibits 4% higher energy absorption compared to Fig. 13a as validated by FE simulations. The GRU-predicted trend of how the tubule orientation angle affects the SEA is shown in Fig. 13c for square porosity. The prediction shows a sinusoidal variation, which is reasonable, as the top-down projected load-bearing area (area unaffected by porosity) varies in a sinusoidal fashion.
3. The structure with maximum and minimum SEA depends upon the volume fraction of the porosity. Further, it is also affected by the strain rate and the orientation of polygonal porosity,

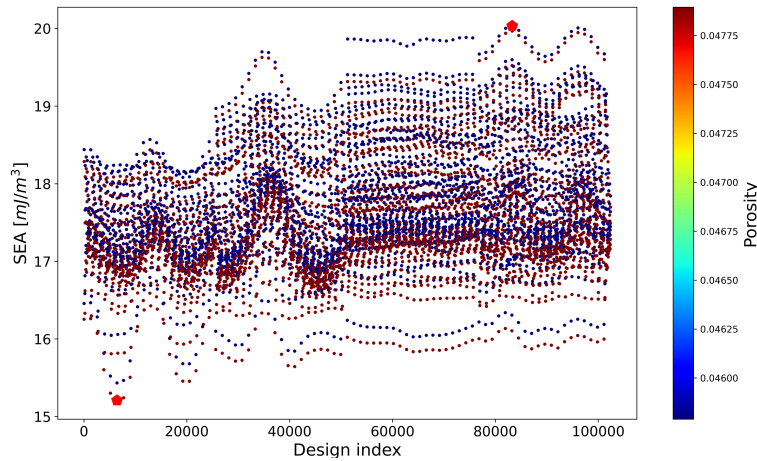


Figure 10: SEA versus Design Index for porosity volume fraction from 4.5% to 5%. The highest and lowest SEA designs are highlighted in solid red pentagons.

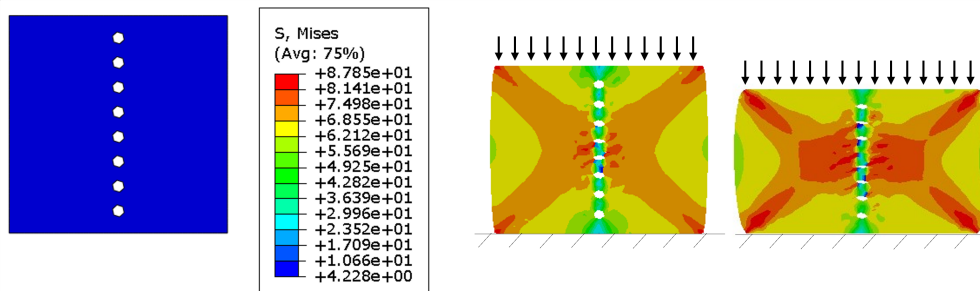


Figure 11: Initial structure (left) with highest predicted SEA and stress distribution at 12.5% and 25% nominal strain (right).

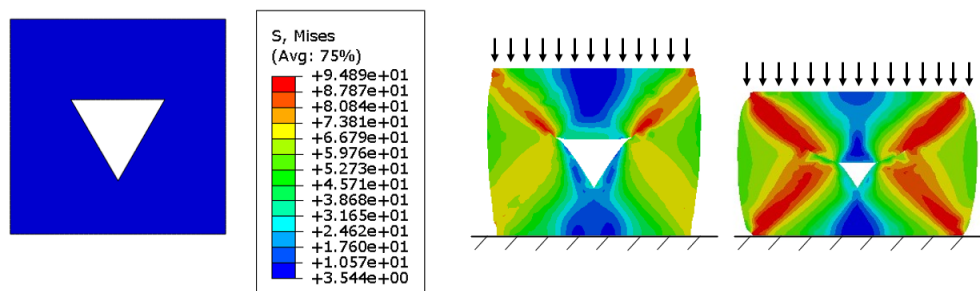


Figure 12: Initial structure (left) with lowest predicted SEA and stress distribution at 12.5% and 25% nominal strain (right).

as shown in Fig. 6. For example, the red mark in Fig. 8, Fig. 9, and Fig. 10 shows different structures (design index) with maximum and minimum SEA.

4. The Pearson correlation coefficient is calculated to assess the relationship between SEA and different geometric parameters. Both cases show a strong negative correlation between SEA and volume fraction, indicating that increasing porosity volume fraction generally leads to decreasing SEA. The correlation coefficients for angle offset are close to zero, consistent

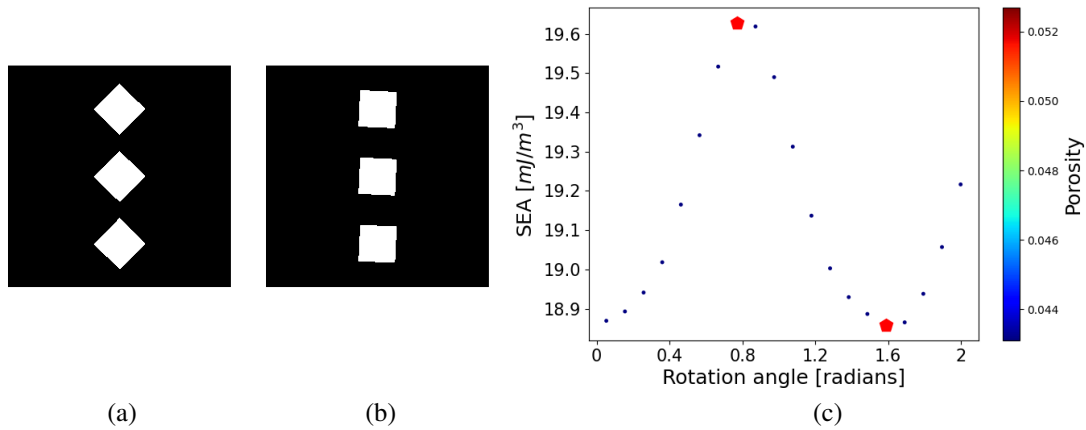


Figure 13: Effect of orientation on energy absorption under transverse compression for constant volume fraction: (a) Structure absorbing less energy. (b) Structure absorbing more energy (c) Predicted trend as the angle offset is varied.

with the sinusoidal nature of the trend observed in Fig. 13. The orientation of pores was found to cause a significant variation in the SEA, that is a difference close to 4%. Hence, in order to conclude correct observations using correlation analysis, it is necessary to employ exploratory grid search methods to identify select designs that exhibit a high SEA. The number of pores in the x-direction is negatively correlated to SEA, while the number of pores in the y-direction is positively correlated. Apart from that, a minor correlation is observed for other variables.

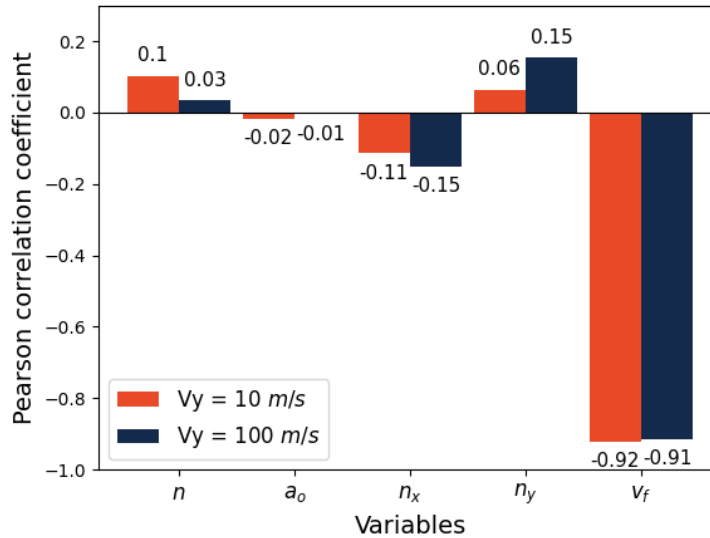


Figure 14: Pearson correlation coefficient between SEA and geometric variables at two different indenter velocities.

4. Conclusions and future work

In this work, a combinatorial framework was developed to generate bio-inspired low-porosity designs with tubules of various shapes, orientations, and in-plane arrangements. The structures

were made from PC-ABS with rate-dependent elastoplastic behavior. FE simulations were conducted to obtain the stress-strain curves of the structures at different impact velocities during transverse loading. Using the FE simulation data, a GRU model was trained to predict the stress-strain curve for low-porosity bio-inspired structures under dynamic transverse compression loading. Data augmentation techniques were implemented to reduce the number of simulations required using Abaqus. The trained NN model could make accurate predictions (MAE: 6.07×10^{-3}) for SEA of all the structures across a range of final strain and strain rates. Further, the trained neural network was used to survey the entire design space with 128000 structures at each strain rate. Overall, the trained model NN was able to generate all the performance predictions on low-end laptops. Stress-strain response for each structure could be predicted in 0.16ms. Hence, it renders itself a suitable preliminary guide in preliminary design stages to quickly survey designs for more detailed analyses. The SEA maps were generated using a grid search based on geometric variables. The structure-property maps facilitated the identification of several design trends and observations obtained from the trained NN model. The study investigated the impact of porosity arrangement, volume fraction, strain rate, and orientation on the SEA of low-porosity structures. The study revealed that varying the orientations of pores can result in approximately 4% difference in SEA. Further, arranging pores vertically at the same volume fraction led to greater SEA. Such SEA maps could also be used to study the effect of design parameters on energy absorption for various loading conditions. The Pearson correlation analysis was also utilized to study the correlation between SEA and other geometric parameters. The results indicated a strong negative correlation between SEA and porosity volume fraction, while minor correlations were observed for other variables. The minor correlation between the variables reinforces the need to utilize exploratory grid searches to identify select configurations that exhibit higher SEA under given loading conditions.

In future work, gradients of the GRU model will be utilized to define an inverse design problem and generate new designs. In the current work, periodic boundary conditions were not enforced on the representative volume when comparing different structures. The effect of enforcing periodic boundary conditions will also be explored in future work.

Data availability

The data and source code that support the findings of this study will be available upon request during the review process, and it will be open source after the publication is online.

Conflict of interest

The authors declare that they have no conflict of interest.

Acknowledgements

We acknowledge the support of the National Science Foundation grant (MOMS-1926353) and the Army Research Office contract (No. W 911NF-18-2-0067).

CRedit author contributions

Shashank Kushwaha: Conceptualization, Methodology, Software, Formal analysis, Investigation, Data Curation, Writing - Original Draft. **Junyan He:** Methodology, Software, Formal

analysis, Writing - Original Draft. **Diab Abueidda:** Supervision, Writing - Review & Editing. **Iwona Jasiuk:** Supervision, Resources, Writing - Review & Editing, Funding Acquisition.

References

- [1] Ngoc San Ha and Guoxing Lu. A review of recent research on bio-inspired structures and materials for energy absorption applications. *Composites Part B: Engineering*, 181:107496, 2020.
- [2] Benjamin S Lazarus, Audrey Velasco-Hogan, Teresa Gómez-del Río, Marc A Meyers, and Iwona Jasiuk. A review of impact resistant biological and bioinspired materials and structures. *Journal of Materials Research and Technology*, 9(6):15705–15738, 2020.
- [3] Marc André Meyers, Po-Yu Chen, Albert Yu-Min Lin, and Yasuaki Seki. Biological materials: Structure and mechanical properties. *Progress in materials science*, 53(1):1–206, 2008.
- [4] Xindi Yu, Longcheng Pan, Jinxiang Chen, Xiaoming Zhang, and Peixing Wei. Experimental and numerical study on the energy absorption abilities of trabecular–honeycomb biomimetic structures inspired by beetle elytra. *Journal of Materials Science*, 54(3):2193–2204, 2019.
- [5] Andrew Kitchener. An analysis of the forces of fighting of the blackbuck (antelope cervicapra) and the bighorn sheep (ovis canadensis) and the mechanical design of the horn of bovids. *Journal of Zoology*, 214(1):1–20, 1988.
- [6] Chao Gong, Zhonghao Bai, Jiyuan Lv, and Linwei Zhang. Crashworthiness analysis of bionic thin-walled tubes inspired by the evolution laws of plant stems. *Thin-Walled Structures*, 157:107081, 2020. ISSN 0263-8231. doi: <https://doi.org/10.1016/j.tws.2020.107081>. URL <https://www.sciencedirect.com/science/article/pii/S0263823120309551>.
- [7] Vicente Francisco González-Albuixech, Marcos Rodríguez-Millán, T Ito, JA Loya, and MH Miguelez. Numerical analysis for design of bioinspired ceramic modular armors for ballistic protections. *International Journal of Damage Mechanics*, 28(6):815–837, 2019.
- [8] Sachin Mishra, Brajesh Tripathi, Sahil Garg, Ajay Kumar, and Pradeep Kumar. Design and development of a bio-inspired flapping wing type micro air vehicle. *Procedia Materials Science*, 10:519–526, 2015. ISSN 2211-8128. doi: <https://doi.org/10.1016/j.mspro.2015.06.001>. URL <https://www.sciencedirect.com/science/article/pii/S2211812815002394>. 2nd International Conference on Nanomaterials and Technologies (CNT 2014).
- [9] Xiaoming Zhang, Juan Xie, Jinxiang Chen, Yoji Okabe, Longcheng Pan, and Mengye Xu. The beetle elytron plate: A lightweight, high-strength and buffering functional-structural bionic material. *Scientific Reports*, 7(1), 2017. doi: 10.1038/s41598-017-03767-w. Cited by: 54; All Open Access, Gold Open Access, Green Open Access.
- [10] L Amorim, A Santos, JP Nunes, and JC Viana. Bioinspired approaches for toughening of fibre reinforced polymer composites. *Materials & Design*, 199:109336, 2021.
- [11] Nicu Toader, Werner Sobek, and Klaus G Nickel. Energy absorption in functionally graded concrete bioinspired by sea urchin spines. *Journal of Bionic Engineering*, 14(2):369–378, 2017. ISSN 1672-6529. doi: [https://doi.org/10.1016/S1672-6529\(16\)60405-5](https://doi.org/10.1016/S1672-6529(16)60405-5).
- [12] Fabian Duddeck, Stephan Hunkeler, Pablo Lozano, Erich Wehrle, and Duo Zeng. Topology optimization for crashworthiness of thin-walled structures under axial impact using hybrid cellular automata. *Structural and Multidisciplinary Optimization*, 54(3):415–428, 2016.
- [13] Junyan He, Shashank Kushwaha, Diab Abueidda, and Iwona Jasiuk. LatticeOPT: a heuristic topology optimization framework for thin-walled, 2D extruded lattices. *Structural and Multidisciplinary Optimization*, 65(11):308, 2022.
- [14] Duo Zeng and Fabian Duddeck. Improved hybrid cellular automata for crashworthiness optimization of thin-walled structures. *Structural and Multidisciplinary Optimization*, 56(1):101–115, 2017.
- [15] Pezhman Sharafi, Lip H Teh, and Muhammad NS Hadi. Shape optimization of thin-walled steel sections using graph theory and aco algorithm. *Journal of Constructional Steel Research*, 101:331–341, 2014.
- [16] Charles Yang, Youngsoo Kim, Seunghwa Ryu, and Grace X Gu. Prediction of composite microstructure stress-strain curves using convolutional neural networks. *Materials & Design*, 189:108509, 2020.
- [17] Chun-Teh Chen and Grace X Gu. Machine learning for composite materials. *MRS Communications*, 9(2):556–566, 2019.
- [18] Diab W. Abueidda, Mohammad Almasri, Rami Ammourah, Umberto Ravaoli, Iwona M. Jasiuk, and Nahil A. Sobh. Prediction and optimization of mechanical properties of composites using convolutional neural networks. *Composite Structures*, 227:111264, 2019. ISSN 0263-8223. doi: <https://doi.org/10.1016/j.compstruct.2019.111264>. URL <https://www.sciencedirect.com/science/article/pii/S0263822319312383>.
- [19] Srinivasu Gangi Setti and RN Rao. Artificial neural network approach for prediction of stress–strain curve of near β titanium alloy. *Rare Metals*, 33:249–257, 2014.
- [20] Junyan He, Seid Koric, Shashank Kushwaha, Jaewan Park, Diab Abueidda, and Iwona Jasiuk. Novel deepnet architecture to predict stresses in elastoplastic structures with variable complex geometries and loads. *arXiv preprint arXiv:2306.03645*, 2023.
- [21] Junyan He, Diab Abueidda, Rashid Abu Al-Rub, Seid Koric, and Iwona Jasiuk. A deep learning energy-based method for classical elastoplasticity. *International Journal of Plasticity*, page 103531, 2023.
- [22] Othman Laban, Samer Gowid, and Elsadig Mahdi. Experimental investigation and uncertainty prediction of the load-carrying capacity of composite double hat for lattice core sandwich panels using artificial neural network. In *2020 IEEE International Conference on Informatics, IoT, and Enabling Technologies (ICIoT)*, pages 67–72. IEEE, 2020.
- [23] Mark C. Messner. Convolutional neural network surrogate models for the mechanical properties of periodic structures. *Journal of Mechanical Design*, 142(2), 10 2019. ISSN 1050-0472. doi: 10.1115/1.4045040. URL <https://doi.org/10.1115/1.4045040>. 024503.
- [24] Hany Hassanin, Yusra Alkendi, Mahmoud Elsayed, Khamis Essa, and Yahya Zweiri. Controlling the properties of additively manufactured cellular structures using machine learning approaches. *Advanced Engineering Materials*, 22(3):1901338, 2020.
- [25] SIMULIA. Abaqus, 2021.
- [26] J McKittrick, P-Y Chen, L Tombolato, EE Novitskaya, MW Trim, GA Hirata, EA Olevsky, MF Horstemeyer, and MA Meyers. Energy absorbent natural materials and bioinspired design strategies: a review. *Materials Science and Engineering: C*, 30(3):331–342, 2010.
- [27] Fabian Pedregosa, Gaël Varoquaux, Alexandre Gramfort, Vincent Michel, Bertrand Thirion, Olivier Grisel, Mathieu Blondel, Peter Prettenhofer, Ron Weiss, Vincent Dubourg, et al. Scikit-learn: Machine learning in Python. *the Journal of machine Learning research*, 12:2825–2830, 2011.
- [28] Cort J Willmott and Kenji Matsuura. Advantages of the mean absolute error (mae) over the root mean square error (rmse) in assessing average model performance. *Climate research*, 30(1):79–82, 2005.

- [29] Junyan He, Shashank Kushwaha, Diab Abueidda, and Iwona Jasiuk. Exploring the structure-property relations of thin-walled, 2D extruded lattices using neural networks. *Computers & Structures*, 277:106940, 2023.
- [30] Diab W Abueidda, Seid Koric, Nahil A Sobh, and Huseyin Sehitoglu. Deep learning for plasticity and thermo-viscoplasticity. *International Journal of Plasticity*, 136:102852, 2021.
- [31] Ari L Frankel, Reese E Jones, Coleman Alleman, and Jeremy A Templeton. Predicting the mechanical response of oligocrystals with deep learning. *Computational Materials Science*, 169:109099, 2019.
- [32] Jaewan Park, Shashank Kushwaha, Junyan He, Seid Koric, Diab Abueidda, and Iwona Jasiuk. Sequential deep learning operator network (s-deeponet) for time-dependent loads. *arXiv preprint arXiv:2306.08218*, 2023.
- [33] Francois Chollet et al. Keras, 2015. URL <https://github.com/fchollet/keras>.
- [34] Martín Abadi, Ashish Agarwal, Paul Barham, Eugene Brevdo, Zhifeng Chen, Craig Citro, Greg S. Corrado, Andy Davis, Jeffrey Dean, Matthieu Devin, Sanjay Ghemawat, Ian Goodfellow, Andrew Harp, Geoffrey Irving, Michael Isard, Yangqing Jia, Rafal Jozefowicz, Lukasz Kaiser, Manjunath Kudlur, Josh Levenberg, Dandelion Mané, Rajat Monga, Sherry Moore, Derek Murray, Chris Olah, Mike Schuster, Jonathon Shlens, Benoit Steiner, Ilya Sutskever, Kunal Talwar, Paul Tucker, Vincent Vanhoucke, Vijay Vasudevan, Fernanda Viégas, Oriol Vinyals, Pete Warden, Martin Wattenberg, Martin Wicke, Yuan Yu, and Xiaoqiang Zheng. TensorFlow: Large-scale machine learning on heterogeneous systems, 2015. URL <https://www.tensorflow.org/>. Software available from tensorflow.org.
- [35] Diederik P Kingma and Jimmy Ba. Adam: A method for stochastic optimization. *arXiv preprint arXiv:1412.6980*, 2014.